Title

Real-Time Visualization of Tissue Surface Biochemical Features Derived from Fluorescence Lifetime Measurements

Journal

IEEE Transactions on Medical Imaging, 35(8)

ISSN

0278-0062

Authors

Gorpas, Dimitris
Ma, Dinglong
Bec, Julien
et al.

Publication Date

2016-08-01

DOI

10.1109/tmi.2016.2530621

Peer reviewed

HHS Public Access

Author manuscript

IEEE Trans Med Imaging. Author manuscript; available in PMC 2016 December 01.

Published in final edited form as:

IEEE Trans Med Imaging. 2016 August ; 35(8): 1802–1811. doi:10.1109/TMI.2016.2530621.

Real-Time Visualization of Tissue Surface Biochemical Features Derived from Fluorescence Lifetime Measurements

Dimitris Gorpas [Member, IEEE],
Department of Biomedical Engineering, University of California Davis, CA 95616 USA

Dinglong Ma,
Department of Biomedical Engineering, University of California Davis, CA 95616 USA

Julien Bec,
Department of Biomedical Engineering, University of California Davis, CA 95616 USA

Diego R. Yankelevich, and
Department of Biomedical Engineering and with the Department of Electrical and Computer Engineering, University of California Davis, CA 95616 USA

Laura Marcu
Department of Biomedical Engineering, University of California Davis, CA 95616 USA

Dimitris Gorpas: dgorpas@ucdavis.edu; Dinglong Ma: dgorpas@ucdavis.edu; Julien Bec: jbec@ucdavis.edu; Diego R. Yankelevich: yankelev@ece.ucdavis.edu; Laura Marcu: lmarcu@ucdavis.edu

Abstract

Fiber based fluorescence lifetime imaging has shown great potential for intraoperative diagnosis and guidance of surgical procedures. Here we describe a novel method addressing a significant challenge for the practical implementation of this technique, i.e. the real-time display of the quantified biochemical or functional tissue properties superimposed on the interrogated area. Specifically, an aiming beam (450 nm) generated by a continuous-wave laser beam was merged with the pulsed fluorescence excitation light in a single delivery/collection fiber and then imaged and segmented using a color-based algorithm. We demonstrate that this approach enables continuous delineation of the interrogated location and dynamic augmentation of the acquired frames with the corresponding fluorescence decay parameters. The method was evaluated on a fluorescence phantom and fresh tissue samples. Current results demonstrate that 34 frames per second can be achieved for augmenting videos of 640×512 pixels resolution. Also we show that the spatial resolution of the fluorescence lifetime map depends on the tissue optical properties, the scanning speed, and the frame rate. The dice similarity coefficient between the fluorescence phantom and the reconstructed maps was estimated to be as high as 93%. The reported method could become a valuable tool for augmenting the surgeon's field of view with diagnostic information derived from the analysis of fluorescence lifetime data in real-time using handheld,

Correspondence to: Dimitris Gorpas, dgorpas@ucdavis.edu; Laura Marcu, lmarcu@ucdavis.edu.

This paper has supplementary material that are available in the supplementary files/multimedia tab. This includes two AVI and one MP4 format movie clips, which show additional results of the proposed methodology. This material is 172.1MB in size.

automated, or endoscopic scanning systems. Current method provides also a means for maintaining the tissue light exposure within safety limits. This study provides a framework for using an aiming beam with other point spectroscopy applications.

Index Terms

Aiming beam; color segmentation; fluorescence lifetime imaging; image overlay; real-time imaging; augmented reality

I. Introduction

Optical spectroscopy and imaging techniques can provide information about structural, biochemical or functional properties of biological tissues. Multimodal imaging approaches have been also implemented to enhance detection of complementary features in tissue. In this context, very recently, emphasis has been placed on the development of visualization methods enabling co-registration of information from distinct imaging modalities by means of real-time augmented reality [1–5]. However, such methods have not been reported for point-scanning spectroscopic imaging techniques. Although scanning techniques have shown potential to provide real-time feedback about the biochemical features of tissue at each measured location [6–10], their clinical implementation is still limited by the difficulty in registering dynamically the diagnostic information derived from optical parameters with the location from where the optical measurement was taken. Scanning multispectral time-resolved fluorescence spectroscopy (ms-TRFS) [9, 11], for example, has demonstrated ability to rapidly characterize and diagnose diseased tissues based on their autofluorescence properties [12–17]. Nevertheless, this technique, as other optical spectroscopy techniques (i.e. diffuse reflectance spectroscopy), lacks an efficient visualization method of the measured quantities, making it prone to registration errors. Registering the diagnostic information is further complicated when wavelengths outside the human eye sensitivity are employed, such as the UV light for excitation of autofluorescence, or the intensity of the emitted light is below the sensitivity of conventional cameras. In such cases, the identification of the measured location is an additional challenge, since the operator cannot visually locate the interrogated area by tracking the incident or emitted light on the tissue surface. A common approach to overcome these challenges is based on off-line data analysis and registration based on structural landmarks or spatial sampling at predefined locations [6, 13, 16].

The goal of this study is to demonstrate a method that makes use of a laser beam in the visible spectrum or aiming beam to address the aforementioned challenges and thus enable a more effective and on-line application of the ms-TRFS in clinical settings. The concept of aiming beam is commonly used in ophthalmological applications for guidance during photocoagulation [18, 19] and safety measure for guidance of laser surgery procedures. The CO_2 laser typically used in such applications is invisible to the human eye [20]. Nevertheless, to our knowledge, the use of an aiming beam for on-line visualization of optical spectroscopy parameters carrying diagnostic information has not been exploited.

This study presents a novel framework compatible with intra-operative use of an aiming beam for online tracking and mapping of tissue biochemical properties. Specifically, we developed and validated a method that i) extracts the aiming beam location from a video stream acquired by a camera and ii) overlays onto those images the fluorescence lifetime values as transparent pseudo-color masks. This provides dynamic visualization of the biochemical information of the measured points. Moreover, these pseudo-color masks can be dynamically updated during the scanning procedure, constructing fluorescence lifetime imaging (FLIm) maps of tissues. The method is particularly well suited to interventions already providing a live video stream of the operating field, such as some endoscopic or robotic assisted interventions and can easily be integrated to free-hand or motorized scanning applications with the addition of a camera to image the regions of interest.

II. Materials And Methods

The data flow of the method reported here is depicted in Fig. 1. It consists of two parallel algorithmic blocks; one enables rapid fluorescence data analysis (including fluorescence transient signals deconvolution and average lifetime estimation), the other enables the aiming beam extraction from conventional white-light images. The results from these two blocks are then combined by a third block, i.e. construction of FLIm maps enabling the real-time display of the acquired video frames augmented with biochemical and/or functional information of the interrogated tissues by means of overlaid FLIm maps.

A. ms-TRFS System with Aiming Beam

The time-domain ms-TRFS system used in this study has been described in details elsewhere [11]. A micro Q-switched laser frequency tripled to 355 nm (Teem Photonics, France, 600 ps pulse width, 2 KHz repetition rate) was used for fluorescence excitation. A single 400 μm core diameter silica fiber (Polymicro Technologies™, USA) was used for fluorescence excitation and collection. The proximal end of the fiber was connected to a wavelength selection module (WSM) composed of a set of dichroic mirrors and band-pass filters that can spectrally resolve the collected signal in four channels simultaneously: 390/40 nm (channel 1), 466/40 nm (aiming beam), 542/50 nm (channel 2), and 629/53 nm (channel 3). For the current study, the second physical channel of the WSM was dedicated to the aiming beam delivery. A 450 nm beam from a continuous-wave diode laser (PL 450B, Osram, Germany) was coupled into this channel and thus the aiming beam was delivered via the same optical path as the fluorescence excitation beam (Fig. 2). The incident power of the aiming beam on the sample was approximately 3 mW. The other three channels were connected to optical fibers of distinct lengths (acting as delay lines) coupled at their distal end into a single microchannel plate photomultiplier tube (MCP-PMT, R3809U-50, Hamamatsu, 45 ps FWHM). The fluorescence signals from the three channels, after being detected by the MCP-PMT and boosted by an RF amplifier (AM-1607-3000, 3 GHz bandwidth, Miteq, USA), were temporally resolved by the digitizer (PXIe-5185, National Instruments, 12.5 GS/s sampling rate) at 80 ps time intervals. The RF amplifier used is AC coupled with a low cut-off frequency of 10 KHz. Therefore, the auto-fluorescence signal induced by the aiming beam (continuous-wave), was filtered-out by the amplifier and was not present in the acquired data.

A CMOS camera (UI144xSE-C, 1280×1024 pixels, 17 fps, IDS GmbH, Germany) was used for imaging the area of interest during the experimental process. The camera software development kit (SDK) was used to set the acquisition parameters and capture the video frames. Nevertheless, the current method can be easily adapted to function with any conventional color camera.

Image analysis and ms-TRFS signal processing algorithms were implemented in C++ using the open source computer vision library OpenCV 3.0 (opencv.org). The PC was equipped with an Intel Core i7-3632QM CPU and 16 GB of RAM. ms-TRFS data acquisition and pre-processing were implemented in the digitizer (Intel Celeron dual-core T3100 CPU, 3 GB RAM) with LabVIEW platform (National Instruments). The communication between the CPU and the digitizer was implemented via a TCP/IP protocol, where the digitizer was serving as the host and the CPU as the client.

B. Aiming Beam Imaging and Segmentation (Block 1)

The algorithmic block 1 concerns the extraction of the location of the aiming beam from each acquired frame (Fig. 1). The wavelength of the aiming beam significantly affects the segmentation process. Shorter wavelengths of the visible spectrum present limited penetration depth and consequently limited diffused reflectance [21, 22]. Such wavelengths would ensure that the projected aiming beam approximates the autofluorescence excitation source profile. In contrary, use of longer wavelengths for the aiming beam would lead to the segmentation of significantly larger areas than the actual areas of incidence of the excitation source. The aiming beam source (450 nm) used in this study has been chosen accordingly.

The segmentation block consists of three processes. First, the acquired frames are transformed from the RGB to the HSV colorspace and thresholded for the hue values that correspond to blue color [23] ($H_{threshold}$: 85–155/H_{Blue} = 120 in OpenCV). To detect a wide range of blue intensities, value and saturation were both bounded between 50 and 255. These values might be subject to refinement when other blue or violet objects are present (e.g. surgical gloves). Application of this threshold to the fresh tissue depicted in Fig. 3a, results into the binary image of Fig. 3b.

Second, the binary images undergo morphological filtering to remove any remaining noise [23, 24]. Specifically, a morphological dilation with a circular structured element of diameter equal to 3 pixels is initially applied to the image. Application of this filter ensures that the aiming beam will not appear broken in the binary image (i.e. a portion of the beam is invisible and appears as multiple small segments). This filter, however, also leads to enlarged noise artifacts. To account for this, denoising is applied through morphological erosion followed by a dilation. A circular structured element with diameter equal to 7 pixels is used in both these filters. Thereafter erosion with a 3 pixels diameter structured element is applied to restore the aiming beam back to its original size. The result of this filtering sequence is shown in Fig. 3c.

Third, each element in the binary image (i.e. aiming beam plus any remaining noise artifacts) is fitted to an ellipse, to approximate the actual shape of the projected aiming beam. For each frame, the Euclidian distance between the center of the current ellipse and

the one from the previous frame is estimated. The ellipse corresponding to the minimum distance is attributed to the aiming beam (Fig. 3d). Any frame where no aiming beam is detected is discarded, the method proceeds to the acquisition of the next frame, and for the new ellipse the Euclidian distance is estimated from the image center.

C. Fluorescence Signal Deconvolution

1) ms-TRFS signal preprocessing—Following the acquisition of each fluorescence transient signal, a background subtraction is applied (i.e. subtraction of a reference signal from the acquired fluorescence transient signals). The reference signal is acquired prior to the measurements and corresponds to the autofluorescence from the fiber. The embedded computer of the digitizer was used for signal preprocessing. TCP/IP sockets are then used to transfer the fluorescence signals to the CPU (Fig. 1).

2) ms-TRFS signal deconvolution (Block 2)—Block 2 concerns the deconvolution of the fluorescence decay signal (Fig. 1). Constrained least-squares deconvolution with Laguerre expansion [25] was used to quantify the fluorescence decay characteristics. In time-domain, the fluorescence decay is usually expressed as follows [26]:

$$y(k) = \sum_{i=0}^{k} I(k-i) \cdot h(k) + \varepsilon_k \quad (1)$$

where N is the number of the equally spaced sampling time points and $k = 0, \ldots, N-1$. In (1) $y(k)$ is the k^{th} measured decay, $I(k)$ is the instrument impulse response function (iIRF) and $h(k)$ the fluorescence impulse response function (fIRF); ε_k represents the additive measurement noise.

Based on the constrained least-squares method described in [25], (1) can be approximated by the matrix formula:

$$\hat{h} = \mathbf{B} \cdot \hat{c} \quad (2)$$

where $\mathbf{B} = [b_0, b_1, \ldots, b_{L-1}]$ are the L discrete time Laguerre basis functions. Moreover, $\hat{c}$ is the vector of the Laguerre coefficients and is approximated as [25]:

$$\hat{c} = \left(V^{-1} \cdot V\right)^{-1} \cdot \left(V^T \cdot y - D^T \cdot \hat{\lambda}\right) \quad (3)$$

where V is the convolution of the iIRF with the Laguerre basis functions, D is the third-order forward finite difference matrix and depends only on the length of the acquired signal vectors. Finally, $\hat{\lambda}$ is the Lagrangian multiplier which is estimated by the non-negative least-squares problem [25]:

$$\min_{\lambda}\left\|C\cdot\left(V^{T}\cdot y-D^{T}\cdot\lambda\right)\right\|^{2},\text{where }\lambda\geq 0 \quad (4)$$

with C being the Cholesky decomposition of the positive definite matrix $(V^{T}\cdot V)^{-1}$.

The matrices in (2) through (4) that are independent of the fluorescence signals can be estimated before any measurement is acquired. The deconvolution is then implemented via the following 3 steps: i) estimation of the Lagrangian multiplier from (4), ii) estimation of the Laguerre coefficients from (3), and iii) estimation of the fIRF from (2). The average lifetime values are approximated from the resulted fIRF as described in [25]. OpenCV functions were used for all the required computations, with the exception of the non-negative least-squares, which was a C++ version of the Lawson-Hanson method [27]. This implementation of the deconvolution algorithm reduces the computational time by approximately 35% (~2.4 ms per decay) when compared with the implementation based on Matlab (Mathworks Inc.) that our group has used in the past (~3.7 ms per decay). Further, this is achieved without any impact on the lifetime estimation accuracy, as expected.

D. Visualization of Lifetime Values Distribution (Block 3)

The third algorithmic block concerns the formation of the displayed frames, which consists of the acquired white-light frames augmented with the FLIm maps. As shown in Fig. 1, this block has two inputs; (i) the location of the ellipse fitted to the aiming beam, and (ii) the corresponding lifetime values for the three WSM channels. This information is combined to create the FLIm maps and overlay them onto the acquired frames as pseudo-color transparent masks.

During scanning, however, consecutive ellipses can partially overlap. This can lead to pixelated lifetime visualization, especially when scanning through fluorescence contrast regions edges. This is addressed by the per pixel weighting of the lifetime corresponding to each ellipse:

$$\tau(u,v,k)=\frac{\tau(u,v,k-1)\cdot[N(u,v)-1]+\tau(u,v,k)}{N(u,v)}\Big|_{CHx} \quad (5)$$

where $\tau(u,v,k)$, is the lifetime for channel CHx, at (u,v) pixel and k^{th} frame. $N(u,v)$ is the accumulated index of how many times pixel (u,v) was visited during the scan. There is a distinct index $N(u,v)$ per channel of the WSM. Combining (5) with the ellipse fitted to the aiming beam, three masks are constructed with the weighted lifetime values (one mask for each WSM channel). These masks are dynamically updated as the scan is progressing.

The FLIm maps (pseudo-color versions of lifetime masks) are also constructed, where the color of each pixel is determined by user defined lower- and upper-bounds of lifetime values. These bounds can be updated online during the scan; an action that instantly updates the entire FLIm maps. User can also select which one of the three channels will be overlaid onto the acquired frames. The overlay is implemented through a weighted sum:

$$\mathbf{I}_{out}(\mathbf{M} \neq 0) = a \cdot \mathbf{I}_{in}(\mathbf{M} \neq 0) + (1-a) \cdot \mathbf{M}(\mathbf{M} \neq 0) \quad (6)$$

where $\mathbf{I}_{in}$ is the acquired frame, $\mathbf{I}_{out}$ is the displayed frame, **M** is the FLIm map of the channel *CHx* and $a = [0,1]$ is the weight factor determining the transparency of the overlaid map. Similarly to (5), the weighted sum is applied only to the pixels visited during the scanning process.

The two images, $\mathbf{I}_{in}$ and $\mathbf{I}_{out}$, are finally combined into one with $(2 \cdot N) \times M$ pixels, with N the columns and M the rows of the acquired frame. This image contains both the white-light version of the scene ($\mathbf{I}_{in}$) and the same white-light version augmented with the selected FLIm map ($\mathbf{I}_{out}$). For the image to fit within a high-definition (HD) monitor, the frames after acquisition are scaled accordingly if the dimension $2 \cdot N$ exceeds the width of HD resolution (1920 pixels).

E. Scaling of the Ellipse Fitted to the Aiming Beam

The distinct tissue optical properties, at the aiming beam (450 nm) and the excitation light (355 nm) wavelengths, result into difference between the area of the imaged aiming beam and the area from where fluorescence is measured. In our previous studies [9, 28], we showed that the area over which fluorescence signals are measured is approximately equal to the size of the fiber core, when the probe-to-target distances are smaller than 3 mm. As expected, though, in Fig. 3d the aiming beam covers a much larger area even though the probe-to-target distance is approximately 2 mm.

To address this mismatch between the incident and imaged beam size, we derived the size of the excitation beam by assuming a Gaussian distribution of the aiming beam's intensity profile. Specifically, this distribution was centered to the center of the ellipse fitted to the aiming beam and its maximum spread was set equal to twice the length of the ellipse's major axis (Fig. 4). The parameters of the Gaussian distribution were approximated by solving the linear system:

$$\begin{bmatrix} Y_0 \\ \vdots \\ Y_{N-1} \end{bmatrix} = \begin{bmatrix} x_0^2 & x_0 & 1 \\ \vdots & \vdots & \vdots \\ x_{N-1}^2 & x_{N-1} & 1 \end{bmatrix} \cdot \begin{bmatrix} P \\ Q \\ R \end{bmatrix} \quad (7)$$

for the white-light frame pixels corresponding to the distribution's maximum spread. In (7) N is the number of pixels, y_i is the natural logarithm of the i^{th} pixel's blue channel intensity, after subtracting the baseline (i.e. minimum value), $x_i = i$ are the one-dimensional pixel coordinates ($i = 0, \ldots, N-1$). Assuming a Gaussian function:

$$y = A \cdot exp\left[-(x-\mu)^2/(2 \cdot \sigma)^2\right] \quad (8)$$

the mean $\mu = -Q/(2 \cdot P)$, variance $\sigma^2 = -1/(2 \cdot P)$ and weight $A = \exp[R - Q^2/(4 \cdot P)]$ can be approximated by solving (7). One example of this fitting is shown in Fig. 4b.

These parameters are then used to dynamically define the size of the ellipse fitted to the aiming beam. Specifically, three widths were used during this study: (i) the full width half maximum (FWHM), (ii) the full width at 75% of the maximum (FW0.75M), and (iii) the full width at 90% of the maximum (FW0.9M) of the Gaussian fit. The ellipse was then scaled by considering the ratio between these three widths and its major axis length. The first width (FWHM) is approximately equal to the major axis of the ellipse fitted to the detected aiming beam (Fig. 4a). The FW0.9M of the Gaussian fit is a typical threshold to extract the peak values of a Gaussian distribution, while the FW0.75M is an intermediate width. These widths can be quantified through the variance of the Gaussian distribution:

$$\mathrm{FW0.XM} = 2 \cdot \sigma \cdot \sqrt{-2 \cdot ln\,(0.\mathrm{X})} \quad (9)$$

where 0.X is percentage of the Gaussian distribution's maximum value for thresholding.

Working with a constant scale of the detected aiming beam can, however, lead to either sparse fluorescence lifetime information overlaid onto the white-light frames or to smooth/blurred FLIm maps due to (5). This problem is demonstrated in Fig. 5. For example, Fig. 5a shows a white-light image from fresh lamb tissue augmented with the FLIm map from the first channel of the WSM and for $v = 2$ mm/s scanning speed. In this case the ellipse fitted to the aiming beam was scaled to the FW0.9M of the Gaussian distribution as resulted from (8). The derived FLIm map is dense and the edges between the lifetime contrast sources are sharp. On the other hand, increasing the scanning speed ($v = 20$ mm/s in Fig. 5b), while the frame rate of the method remains constant, results in a sparse FLIm map (Fig. 5b). This can be addressed by using larger ellipses (Fig. 5c and Fig. 5d). The improved coverage for higher scanning speeds is obtained at the cost of a reduced spatial resolution of the constructed FLIm maps.

Thus, there should be a compromise between speed, algorithm frame rate, and spatial resolution. To address this compromise, the ellipse fitted to the aiming beam is automatically scaled based on the following three rules:

$$E = \begin{cases} E_{FW0.9M} + E_{FW0.75M}\,(E_{FW0.9M} = 0), & \text{if } d \le D_{FW0.9M} \\ E_{FW0.75M} + E_{FWHM}\,(E_{FW0.75M} = 0), & \text{if } D_{FW0.9M} < d \le D_{FW0.9M} \\ E_{FWHM}, & \text{else} \end{cases} \quad (10)$$

where E are the FLIm maps and are constructed for all scales, d is the Euclidian distance between the centers of ellipses from two sequential frames, and D is the major axis length of the current ellipse. In case no aiming beam is detected for a certain frame, then this frame is discarded and for the following one distance d is estimated from the image center.

F. Multi-Threading Architecture

To increase the time efficiency of the current method we took advantage of the multi-threading capabilities of modern CPUs that allow for the parallelization of most processes within Blocks 1 and 2 (Fig. 1).

Two key points were considered when designing the multi-threading algorithm. First is the parallel acquisition of the image frame and the ms-TRFS data, which ensures that both modalities are synced. The second is the parallelization of processes that can slow the overall speed under sequential implementation. Under the current architecture (described below), the speed is determined by the slowest process and not by the accumulated time of all processes. This was achieved by introducing a two frames latency.

Specifically, for the first iteration one thread is dedicated to the first frame acquisition and a second thread to the corresponding ms-TRFS signal acquisition and deconvolution. For the second iteration the second frame is acquired at one thread, the corresponding ms-TRFS signal is acquired and deconvolved at a second frame, and the previous frame is segmented at a third frame. These two iterations correspond to the two frames latency. Starting with the third iteration the multi-threading architecture includes the following threads: (i) one for acquisition of the current frame, (ii) one for acquisition and deconvolution of the corresponding ms-TRFS signal, (iii) one for segmentation of the previous frame, (iv) three for construction of the FLIm maps (i.e. one per WSM channel) of the data acquired two iterations before the current, and (v) one for data saving (i.e. video sequence, lifetime values). After all thread workers are completed, the weighted sum between the FLIm maps and the corresponding white-light frames is formed based on (6).

G. Evaluation of the Online Visualization Method

Current method was evaluated for three main algorithmic aspects as described in the following. For all measurements the camera was set at 30 fps, with a resolution of the white-light images equal to 640×512 pixels. Since the FLIm maps depend on the aiming beam tracking, they always cover a sub-region of the acquired white-light images depending on the scanning areas.

1) Evaluation of FLIm maps' spatial resolution—The spatial resolution of the FLIm maps was assessed and quantified based on motorized raster scanning measurements on a custom-made fluorescence phantom. The scanning was implemented over a 13 mm × 13 mm area with speed $v = 1$ mm/s and raster pitch (distance between adjacent scan lines) $dy = 0.5$ mm. The phantom was made by mixing 8 mL casting resin (Clear-Lite, TAP Plastic) with 10 μM laser dye (Coumarin 440, Exciton) as fluorophore, 0.2 grams graphite powder as absorber, and 0.2 grams Silicon dioxide powder (S5631, Sigma-Aldrich) as scatterer. The casting resin was cured with liquid catalyst (Methyl Ethyl Ketone Peroxide, TAP Plastic) to form a solid circular substrate, which was machined to create a 1 mm depth stripe pattern (Fig. 6). The fluorescence lifetime value recovered from the first channel of the system (390/40 nm) was equal to ~1.6 ns. No signal was detected at the other two channels. To provide fluorescence lifetime contrast, the stripe pattern was filled with 0.05 grams vaseline (Vaseline Petroleum Jelly) mixed with 0.1 grams graphite powder. The fluorescence lifetime

value recovered from the first channel of the system was equal to ~6.5 ns. No signal was detected from the other two channels. In addition, the fluorescence signal amplitude from the phantom was significantly higher than the signal amplitude measured from the mixture, which can be attributed to the different fluorophores, quantum yields and absorber concentrations.

These motorized raster scanning measurements were made considering ellipses that corresponded to the FWHM, and FW0.9M of the Gaussian fit described above. The impact of the ellipse's scale and the pixel averaging from (5) on the estimation of the lifetime values, was quantified through the mean absolute percentage error (MAPE):

$$\mathrm{MAPE}=\frac{1}{N}\cdot\sum_{i=1}^{N}\left|\frac{\tau_i-\hat{\tau}_i}{\tau_i}\right|\times 100\% \quad (11)$$

where τ_i are the real and $\hat{\tau}_i$ he approximated lifetime values, and N the total number of analyzed decays from the entire measured area.

To quantify the spatial accuracy of the method, the stripes of the phantom were segmented by thresholding the FLIm maps at ~3.2 ns for the first channel of the WSM (i.e. twice the lifetime value of the phantom). All pixels with values smaller than this threshold were assumed to belong to the phantom and the rest of the pixels to the stripe pattern. The dice similarity coefficient

$$D=\frac{2\cdot\mathbf{I}_{str}\cap\mathbf{I}_{fl}}{\mathbf{I}_{str}+\mathbf{I}_{fl}} \quad (12)$$

was used to assess the special accuracy. In (12) $\mathbf{I}_{str}$ is the stripe pattern in the white-light image, and $\mathbf{I}_{f}$ the stripe pattern as segmented from the FLIm map.

2) Imaging of fresh tissue samples—Motorized and free-hand scanning measurements were acquired from fresh porcine and lamb tissue samples for various scanning speeds and areas. These measurements were made in order to demonstrate the functionality of the current method (i.e. motorized raster scanning, free-hand scanning), as well as its capability to enable visualization of localized distinct sources of lifetime contrast in biological tissues (i.e. fat, muscle, bone).

The motorized raster scanning measurements were made on porcine tissue samples, with ellipses corresponding to the FWHM, FW0.75M, and FW0.9M of the Gaussian fit described above, as well as automated scaling of the ellipse fitted to the aiming beam. The imaged area for all measurements was equal to 20 mm × 25 mm and the scanning speeds ranged from v = 2 mm/s up to v = 30 mm/s with a raster pitch equal to dy = 0.5 mm. Through these measurements the impact of the ellipse's automated scaling on the construction of the FLIm maps was demonstrated and compared to the fixed scaling.

The robustness of the method to provide the same FLIm maps regardless of the scanning mode (motorized raster or free-hand scanning) was demonstrated with measurements on the fresh lamb tissue samples. The motorized raster scanning measurements were acquired from a 25 mm × 25 mm region with speed $v = 6$ mm/s and vertical step $dy = 0.5$mm.

3) Evaluation of method's frame rate—Finally, the frame rate of the method was evaluated through measurements on the fresh tissues samples described above. The frame rate was quantified for the method's key processes (i.e. aiming beam segmentation, fluorescence transient signal deconvolution, and construction of FLIm maps), and a comparison between the multi-threading versus the sequential algorithmic architectures was implemented.

III. Results and Discussion

A. Spatial Resolution of FLIm maps

The partial overlay of the FLIm maps at 390/40 nm onto the fluorescence phantom is depicted in Fig. 7 for the ellipse fitted to the aiming beam constantly scaled at FWHM (Fig. 7a), and FW0.9M (Fig. 7b). The white-light images of the phantom have undergone contrast enhancement, and cropped to better visualize the stripes of the pattern (bottom half of Fig. 7a and Fig. 7b).

The overlays in Fig. 7a and Fig. 7b demonstrate the impact of ellipse's scale onto the FLIm maps. Specifically, the larger size of the ellipse (Fig. 7a) results into smoothed FLIm maps. In contrast, the smaller size (Fig. 7b) results in sharper FLIm maps. This effect can be further visualized in the corresponding plots (Fig. 7c) depicting the lifetime distribution along a cross-sectional line perpendicular to the fluorescent stripes. The FWHM scale results into a smoother transition between the phantom and the fluorescent stripes, when compared to the FW0.9M scale.

In addition to the spatial resolution of the FLIm maps, the pixel averaging described in (5), in conjunction with the ellipse's scaling, also impacts the lifetime values consisting the maps. Specifically, the phantom has significantly higher signal amplitude than the stripe pattern. Thus the averaging of lifetime values through (5) under the FWHM scale is weighted towards the fast decay of the phantom (~1.6 ns), rather than the slow decay of the fluorescence stripes (~6.5 ns). This is demonstrated in Fig. 7c and Fig. 7d. Specifically, although the width of the second stripe from the left is equal to 800 μm (Fig. 6b) its lifetime values are strongly affected by (5) and the ellipse's scale for Fig. 7c and by the fiber's diameter for Fig. 7d. On the other hand, the phantom lifetime values between the last two stripes are significantly less affected in either the FLIm maps or the measured locations, although the width of this area is approximately 200 μm (Fig. 6b).

The impact of the pixels averaging through (5) on the spatial resolution of the FLIm maps was quantified through the dice similarity coefficient between the resulted from the FLIm maps binary images and the true shape of the pattern. This coefficient was 86% for the FWHM scale and 93% for the FW0.9M one. For this specific phantom these statistical figures mean that despite the smoothing effect introduced, it is possible to recover, with high

accuracy, fluorescence lifetime contrast sources from the constructed FLIm maps, even for the FWHM scale. In addition, the MAPE between the lifetime values of the FLIm maps and the real lifetime values (1.6 ns for the phantom and 6.5 ns for the fluorescent stripes) was equal to 20% for the FWHM scale and 11% for the FW0.9M one. Nevertheless, this is an average error, as the resulted lifetime values at fluorescence contrast transition areas strongly depend on the optical properties of the distinct fluorophores causing the localized error to vary accordingly.

Based on these statistical figures, it is expected that the automated scaling of the ellipse fitted to the aiming beam will result into FLIm maps representing spatial resolution and lifetime values accuracy equivalent to the aforementioned margins, depending on the scanning speed, the method's frame rate and the tissue optical properties.

B. Imaging of Fresh Tissue Samples

Representative results from measurements on the fresh porcine tissue and for all four scales of the ellipse fitted to the aiming beam (FWHM, FW0.75M, FW0.9M, and automated scale) are shown in Fig. 8. In these measurements, the combination of the scanning speed, the ellipse's scale and the method's frame rate define the spatial resolution of the FLIm maps. Specifically, using the FWHM scale (Fig $8a_1$ through Fig. $8a_4$) it can be observed that full coverage is obtained at any speed but the spatial resolution is poor due to the impact of the pixel averaging (5). For this reason, thresholding the Gaussian fit at a lower level than the 50% was not considered, as it would increase even further the blurring impact of (5). Conversely, using the FW0.9M scale (Fig. $8c_1$ through Fig. $8c_4$) low speed scans provide improved spatial resolution at the cost of an incomplete coverage when the scanning speed increases (Fig. $8c_3$ and Fig. $8c_4$). It is expected that thresholding the Gaussian fit at a higher level will not improve significantly the spatial resolution of the FLIm maps, while at the same time it would increase their sparsity even for low scanning speeds. The FW0.75M scale (Fig. $8b_1$ through Fig. $8b_4$) provides intermediate results. Using the automatically adaptive scaling of the ellipse fitted to the aiming beam (Fig. $8d_1$ through Fig. $8d_4$) provides high resolution FLIm maps at low scanning speeds with full coverage at the higher scanning speeds. The scanning process resulted in Fig. $8d_3$ has been recorded in the first attached video file (clip1).

Two representative screenshots from motorized and handheld scanning as seen in the GUI display window are shown in Fig. 9a and Fig. 9b for the 390/40 nm (channel 1) and 540/50 nm (channel 2) bands of the WSM. Both screenshots were captured during the same scanning session on fresh lamb tissue. The displayed channel of the WSM can be changed online during the scanning. The FLIm maps pseudo-color range can be also updated online during the scanning procedure. As seen in Fig. 9a, additional information about the scanning process, such as the processing and camera frame rates (top left of the display window), the processed and skipped frames (bottom right), and the channel currently displayed (top left of the augmented image), is further displayed in the GUI. Finally, a different transparency level is applied between Fig. 9a and Fig. 9b, and can also be changed online during the scanning measurements. The entire scan of Fig. 9a has been recorded in the second attached video file (clip2).

Besides motorized raster scanning applications, the proposed method was also tested with hand-held scanning. Fig. 9c depicts one representative screenshot from hand-held scanning measurements on the fresh lamb tissue sample. The entire scanning process was recorded in the third attached video file (clip3). As mentioned above, the presence of the purple glove in the imaging scene required refinement of the saturation parameter of the HSV thresholding. In this case, a saturation lower limit equal to 150 was adequate for completely removing the glove area from the binary image.

C. Speed of the Visualization Method

To assess the speed of the proposed method, the timing of all major algorithmic blocks was evaluated. The outcomes for two frame resolutions (1280×1024 and 640×512 pixels) are summarized in Table I.

From this analysis three significant observations arise. The first concerns the true speed of the current method (encompassing the time from data acquisition to the deconvolution of ms-TRFS signals). This time (Table I) is shorter than the typical video rate of 30 fps even at the maximum resolution of the camera. Such speed became feasible via the adopted multi-threading architecture. If all these processes were implemented serially, the equivalent speed would be approximately 13 fps for the 1280×1024 and 18 fps for the 640×512 pixels resolution.

The second concerns the overall processing speed of the reported method. This is limited by the display function, which according to OpenCV's documentation (http://docs.opencv.org) is further limited by the size of the images, the monitor refresh rate, and the background processes of the operating system. This limitation can be encountered by skipping frames during the display process. For example, when displaying every second acquired frame the total speed of the method increases to 40 fps and 32 fps for the 640×512 and 1280×1024 resolutions, correspondingly.

The third concerns the ability to rapidly acquire and deconvolve the acquired time-resolved fluorescence signals and to approximate the decay characteristics (i.e. average lifetime values) that allow for online real-time feedback on tissue biochemical and/or functional properties. While our group has previously applied the constrained least-squares deconvolution with Laguerre expansion [13, 25, 29, 30], its applicability for real-time analysis of decay characteristics has not been fully explored. In this study, we modified this deconvolution method to allow for real-time applications in conjunction to the aiming beam tracking method. The speed of deconvolution is approximately 2.4 ms per decay, which corresponds to 7.2 ms for the three decays acquired from each location of the scanning process. The signal acquisition, preprocessing and TCP/IP transmittance time is equal to 9.5 ms and is added to the deconvolution time. Thus the current method requires approximately 16.7 ms (or ~60 fps) for each location of the aiming beam to estimate the three lifetime values.

Adaptation of faster methods for the fluorescence lifetime values estimation (e.g. phasor analysis [31, 32]) is expected to not improve the overall speed of displaying the augmented video frames. Due to parallelization of the processes the overall speed is determined by the

formation of the FLIm maps (Table I). Nevertheless, translation from multi-channel lifetime values display to real-time display of clustering results might benefit from faster lifetime estimation techniques.

Finally, the overall frame rate of the developed method is defined by the slowest between the camera frame rate and the total processing speed. Specifically, for both cases in Table I, the final frame rate of the displayed white-light video stream augmented with the FLIm maps is defined by the camera frame rate (i.e. 17 fps at 1280×1024 pixels and 30 fps at 640×512 pixels).

IV. Conclusions

This study introduces a new framework for the use of an aiming beam for tracking information derived from point measurements in medical imaging applications. To our knowledge, this study is the first to demonstrate the use of an aiming beam as means to overlay optical data that caries diagnostic information onto a wide field image of tissue.

Current results (e.g. Fig. 7 through Fig. 9) demonstrate the use of current method to visually differentiate various lifetime contrast sources. In addition, the scale of the ellipse fitted to the aiming beam is dynamically and automatically adjusted based on the scanning speed, the tissue optical properties, the probe-to-target distance, and the frame rate of the method, optimizing both resolution and coverage of the reconstructed FLIm maps. Finally, we observed (e.g. Fig. $8d_4$) that the spatial sampling obtained for the highest scanning speed of $v = 30$ mm/s does not lead to a significant loss of features in the reconstructed FLIm map.

Future work includes the adaptation of this technique in preclinical and clinical studies. It is expected to provide significant improvement in the detection and biochemical characterization of diseased tissues, as the regions of interest would be delineated through the FLIm maps in real-time. One example is the use of lifetime measurements for breast cancer margins assessment [33] in tissue specimens, where the aiming beam could be used to visualize the tumor margins, either as FLIm maps or as classification results. In addition specific in-vivo applications such as real-time delineation of head and neck cancer during surgery, where motion artifacts are minimal, can benefit from current method. Applications where such artifacts are present will require further implementation of methods that account for potential tissue movement.

In ms-TRFS measurements one significant prerequisite is the compliance with the ANSI limit for UV exposure. Nevertheless, during scanning, it is very challenging to assess that the exposure of each point is within this limit. The method reported here can address this challenge by indexing how many times each pixel has been visited, regardless of the selected WSM active channel. If this index exceeds a certain limit these pixels can be highlighted to show the operator that the area should not be further exposed. Our goal is to link this feature with the actual repetition rate of the excitation source, and thus provide a realistic estimation of the maximum permissive exposure during surgical procedures.

This framework, although developed for and tested with ms-TRFS measurements, can be easily adopted to any other point scanning measurements. In addition, it does not require any

specialized image acquisition modality. It can be used with any available system that provides online video stream of the area of interest, like the stereoscopes in most laparoscopic or surgical robotic systems. Thus current method can enable real-time comprehensive visualization of tissue properties derived from optical measurements, making it highly amendable for clinical use.

Supplementary Material

Refer to Web version on PubMed Central for supplementary material.

Acknowledgments

The authors would like to thank Dr. Jinyi Qi for his comments and suggestions during the development of the algorithms and Dr. Sebastian Dochow for his help during the optimization of the WSM to include the aiming beam source.

This work was supported in part by the National Health Institute Grants: R01 CA187427 and R21 CA178578.

References

1. Ntourakis D, Memeo R, Soler L, Marescaux J, Mutter D, Pessaux P. Augmented Reality Guidance for the Resection of Missing Colorectal Liver Metastases: An Initial Experience. World J Surg. 2015:1–8. [PubMed: 25008243]
2. Yang L, Wang J, Ando T, Kubota A, Yamashita H, Sakuma I, Chiba T, Kobayashi E. Vision-based endoscope tracking for 3D ultrasound image-guided surgical navigation. Comput Med Imag Graph. 2015; 40(2015):205–216.
3. Pessaux P, Diana M, Soler L, Piardi T, Mutter D, Marescaux J. Robotic duodenopancreatectomy assisted with augmented reality and real-time fluorescence guidance. Surg/Endosc. 2014; 28(8): 2493–2498.
4. de Boer E, Harlaar NJ, Taruttis A, Nagengast WB, Rosenthal EL, Ntziachristos V, van Dam GM. Optical innovations in surgery. Br J Surg. 2015; 102(2):e56–e72. [PubMed: 25627136]
5. Venugopal V, Park M, Ashitate Y, Neacsu F, Kettenring F, Frangioni JV, Gangadharan SP, Gioux S. Design and characterization of an optimized simultaneous color and near-infrared fluorescence rigid endoscopic imaging system. J Biomed Opt. 2013; 18(12):126018–126018. [PubMed: 24362927]
6. Brown JQ, Bydlon TM, Richards LM, Yu B, Kennedy Sa, Geradts J, Wilke LG, Junker M, Gallagher J, Barry W, Ramanujam N. Optical assessment of tumor resection margins in the breast. IEEE J Sel Top Quantum Electron. 2010; 16(3):530–544. [PubMed: 21544237]
7. Huang H, Yang L-M, Bai S, Liu J. Smart surgical tool. J Biomed Opt. 2015; 20(2):028001.
8. Khmaladze A, Kuo S, Kim RY, Matthews RV, Marcelo CL, Feinberg SE, Morris MD. Human Oral Mucosa Tissue-Engineered Constructs Monitored by Raman Fiber-Optic Probe. Tissue Eng Part C: Methods. 21(1):46–51. 2014.
9. Ma D, Bec J, Gorpas D, Yankelevich DR, Marcu L. Technique for real-time tissue characterization based on scanning multispectral fluorescence lifetime spectroscopy (ms-TRFS). Biomed Opt Express. 2015; 6(3):987–1002. [PubMed: 25798320]
10. Keller MD, Vargis E, de Matos Granja N, Wilson RH, Mycek MA, Kelley MC, Mahadevan-Jansen A. Development of a spatially offset Raman spectroscopy probe for breast tumor surgical margin evaluation. J Biomed Opt. Jul.2011 16(7):077006. [PubMed: 21806286]
11. Yankelevich DR, Ma D, Liu J, Sun Y, Sun Y, Bec J, Elson DS, Marcu L. Design and evaluation of a device for fast multispectral time-resolved fluorescence spectroscopy and imaging. Rev Sci Instrum. 2014; 85(3):034303. [PubMed: 24689603]
12. Sharma V, Shivalingaiah S, Peng Y, Euhus D, Gryczynski Z, Liu H. Auto-fluorescence lifetime and light reflectance spectroscopy for breast cancer diagnosis: potential tools for intraoperative margin detection. Biomed Opt Express. 2012; 3(8):1825–40. [PubMed: 22876347]

13. Fatakdawala H, Poti S, Zhou F, Sun Y, Bec J, Liu J, Yankelevich DR, Tinling SP, Gandour-Edwards RF, Farwell DG, Marcu L. Multimodal in vivo imaging of oral cancer using fluorescence lifetime, photoacoustic and ultrasound techniques. Biomed Opt Express. 2013; 4(9):1724–1741. [PubMed: 24049693]
14. Marcu L, Hartl BA. Fluorescence lifetime spectroscopy and imaging in neurosurgery. IEEE J Sel Top Quantum Electron. 2012; 18(4):1465–1477.
15. Marcu L. Fluorescence Lifetime Techniques in Medical Applications. Ann Biomed Eng. 2012; 40(2):304–331. [PubMed: 22273730]
16. Sharma V, Olweny EO, Kapur P, Cadeddu JA, Roehrborn CG, Liu H. Prostate cancer detection using combined auto-fluorescence and light reflectance spectroscopy: ex vivo study of human prostates. Biomed Opt Express. 2014; 5(5):1512–1529. [PubMed: 24877012]
17. Coda S, Thompson AJ, Kennedy GT, Roche KL, Ayaru L, Bansi DS, Stamp GW, Thillainayagam AV, French PMW, Dunsby C. Fluorescence lifetime spectroscopy of tissue autofluorescence in normal and diseased colon measured ex vivo using a fiber-optic probe. Biomed Opt Express. 2014; 5(2):515–538. [PubMed: 24575345]
18. Sungwook Y, MacLachlan RA, Riviere CN. Toward automated intraocular laser surgery using a handheld micromanipulator. Intelligent Robots and Systems (IROS 2014), 2014 IEEE/RSJ International Conference on. 2014:1302–1307.
19. Kozak I, Oster SF, Cortes MA, Dowell D, Hartmann K, Kim JS, Freeman WR. Clinical Evaluation and Treatment Accuracy in Diabetic Macular Edema Using Navigated Laser Photocoagulator NAVILAS. Ophthalmology. 2011; 118(6):1119–1124. [PubMed: 21269701]
20. Gofrit ON, Khalaileh A, Ponomarenko O, Abu-Gazala M, Lewinsky RM, Elazary R, Shussman N, Shalhav A, Mintz Y. Laparoscopic Partial Nephrectomy Using a Flexible CO(2) Laser Fiber. JSLS-J Soc Laparoendosc Surg. 2012; 16(4):588–591.
21. Wilson BC, Jacques SL. Optical reflectance and transmittance of tissues: principles and applications. IEEE J Quantum Electron. 1990; 26(12):2186–2199.
22. Benson DM, Knopp JA. Effect of tissue absorption and microscope optical parameters on the depth of penetration fro fluorescence and reflectance measurements of tissue samples. Photochem Photobiol. 1984; 39(4):495–502. [PubMed: 6728921]
23. Gonzalez, RC.; Woods, RE. Digital image processing. 3rd. Upper Saddle River, N.J.: Prentice Hall; 2008.
24. Bovik, AC. Handbook of image and video processing. 2nd. Amsterdam; Boston, MA: Elsevier Academic Press; 2005.
25. Liu J, Sun Y, Qi J, Marcu L. A novel method for fast and robust estimation of fluorescence decay dynamics using constrained least-squares deconvolution with Laguerre expansion. Phys Med Biol. 2012; 57(4):843–65. [PubMed: 22290334]
26. Lakowicz, JR. Principles of Fluorescence Spectroscopy. 3rd. New York: Springer; 2006.
27. Lawson CL, Hanson RJ. Solving Least Squares Problems: Society for Industrial and Applied Mathematics. 1974
28. Papaioannou T, Preyer NW, Fang Q, Brightwell A, Carnohan M, Cottone G, Ross R, Jones LR, Marcu L. Effects of fiber-optic probe design and probe-to-target distance on diffuse reflectance measurements of turbid media: an experimental and computational study at 337 nm. Appl Optics. 2004; 43(14):2846–2860.
29. Fatakdawala H, Gorpas D, Bishop J, Bec J, Ma D, Southard J, Margulies K, Marcu L. Fluorescence Lifetime Imaging Combined with Conventional Intravascular Ultrasound for Enhanced Assessment of Atherosclerotic Plaques: an Ex Vivo Study in Human Coronary Arteries. J Cardiovasc Transl Res. 2015; 8(4):253–263. [PubMed: 25931307]
30. Liu, J.; Elson, DS.; Marcu, L. Fluorescence Lifetime Spectroscopy and Imaging. CRC Press; 2014. Analysis of time-domain fluorescence measurements using least-squares deconvolution; p. 249-268.
31. Digman, MA.; Gratton, E. Fluorescence Lifetime Spectroscopy and Imaging. CRC Press; 2014. The phasor approach to fluorescence lifetime imaging: Exploiting phasor linear properties; p. 235-248.

32. Fereidouni F, Bader AN, Colonna A, Gerritsen HC. Phasor analysis of multiphoton spectral images distinguishes autofluorescence components of in vivo human skin. J Biophotonics. 2014; 7(8): 589–596. [PubMed: 23576407]

33. Gorpas D, Fatakdawala H, Zhang Y, Bold R, Marcu L. Fluorescence lifetime spectroscopy for breast cancer margins assessment," in Optical Biopsy XIII: Toward Real-Time Spectroscopic Imaging and Diagnosis. Proc SPIE. 2015:93180B.

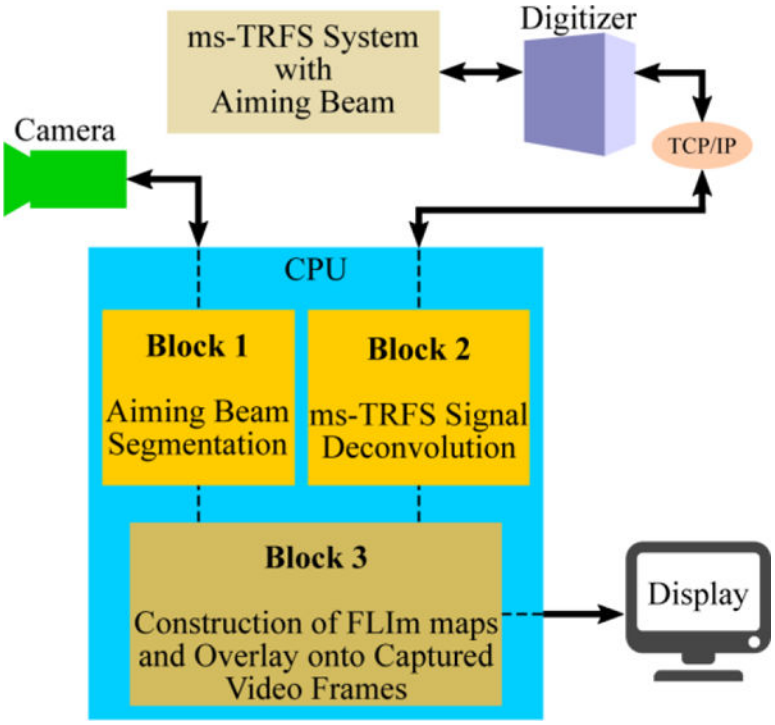

Fig. 1.

The data flow of the developed method. Fluorescence signals are transmitted from the digitizer to the CPU through TCP/IP sockets and undergo a deconvolution process for the estimation of lifetime values. The locations of the measurements are identified by segmentation of the captured video frames. The two blocks are implemented in parallel and their results are combined to overlay the FLIm maps onto the corresponding video frames.

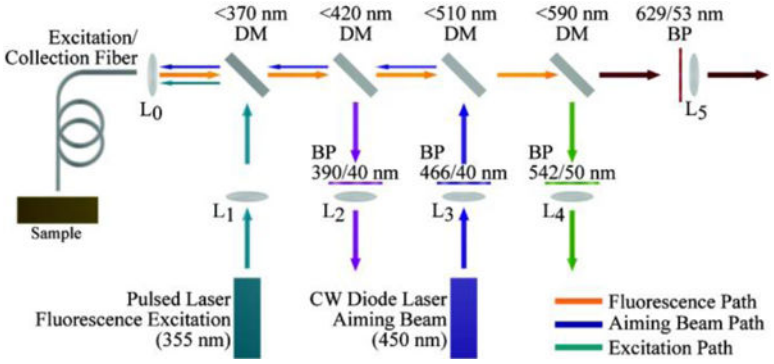

Fig. 2.

Schematic of the modified wavelength selection chamber [11] used in this study, including the single excitation/collection fiber and the aiming beam source. DM: dichroic mirror; BP: bandpass filter; L_i: lens.

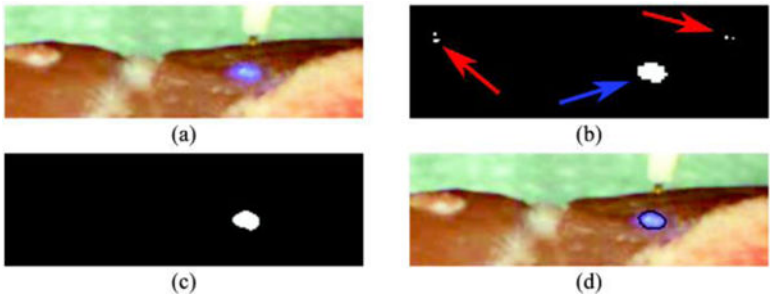

Fig. 3.

Section of an RGB frame displaying the aiming beam projected on a tissue sample (a) and the result of the color-based thresholding (b). The aiming beam is indicated with the blue arrow and the noise structure with the red ones. Morphological filtering is applied for image denoising (c), and the aiming beam is fitted to an ellipse to approximate its actual shape (d).

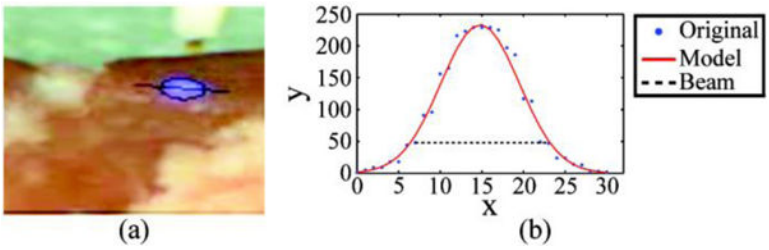

Fig. 4.

The Gaussian distribution's maximum spread equal to twice the length of the ellipse's major axis (a) and the Gaussian fit of the blue channel's intensity values of the corresponding pixels (b). The dashed line is the major axis of the ellipse fitted to the segmented aiming beam.

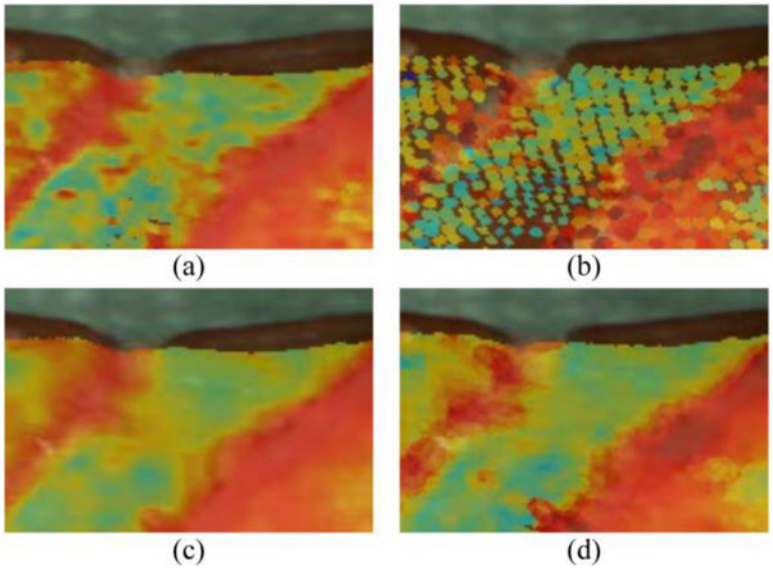

Fig. 5.

White-light images from fresh lamb tissue, augmented with FLIm maps from the first channel of the WSM for the FW0.9M, (a) and (b), and FWHM, (c) and (d), scales of the ellipse fitted to the aiming beam and for $v = 2$ mm/s, (a) and (c), and $v = 20$ mm/s, (b) and (d), scanning speeds. Lifetime values are bounded between 2 ns (blue) and 7 ns (red). Images were cropped and enlarged for optimized visualization.

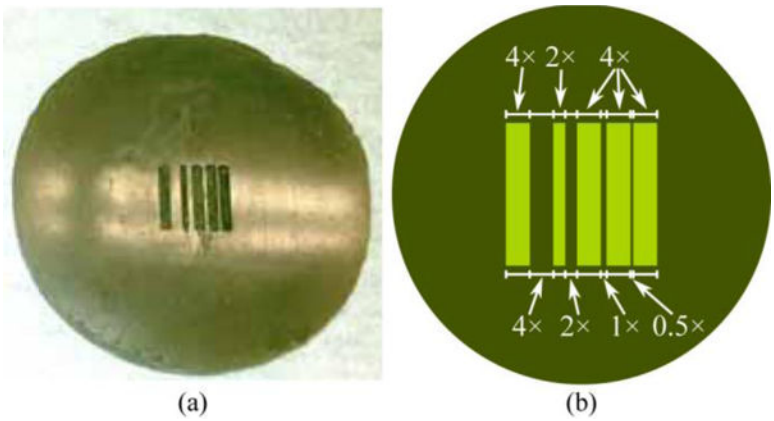

Fig. 6.

The fluorescence phantom as acquired from the camera (a). The dimensions of the stripe pattern (b) are relative to the diameter of the fiber core (400 μm).

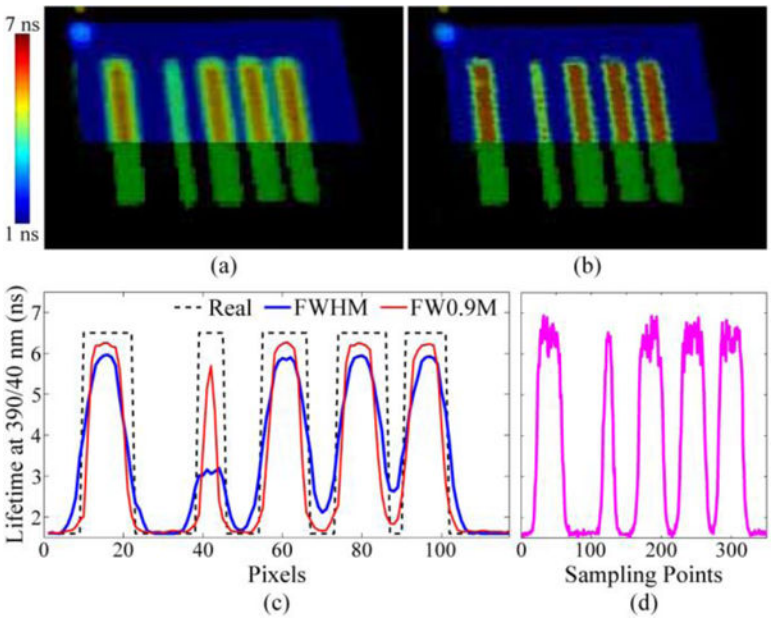

Fig. 7.

FLIm maps at 390/40 nm overlaid (upper areas) onto the contrast enhanced white-light images of the fluorescence phantom for an aiming beam scaled at FWHM (a), and FW0.9M (b) of the Gaussian fit. The light blue spot on top left corner is the aiming beam projection. The corresponding lifetime distributions at a cross-section of the pattern as visualized through the FLIm maps (c), and as measured during the scanning process (d), demonstrate the smoothing impact of the applied ellipse's scale.

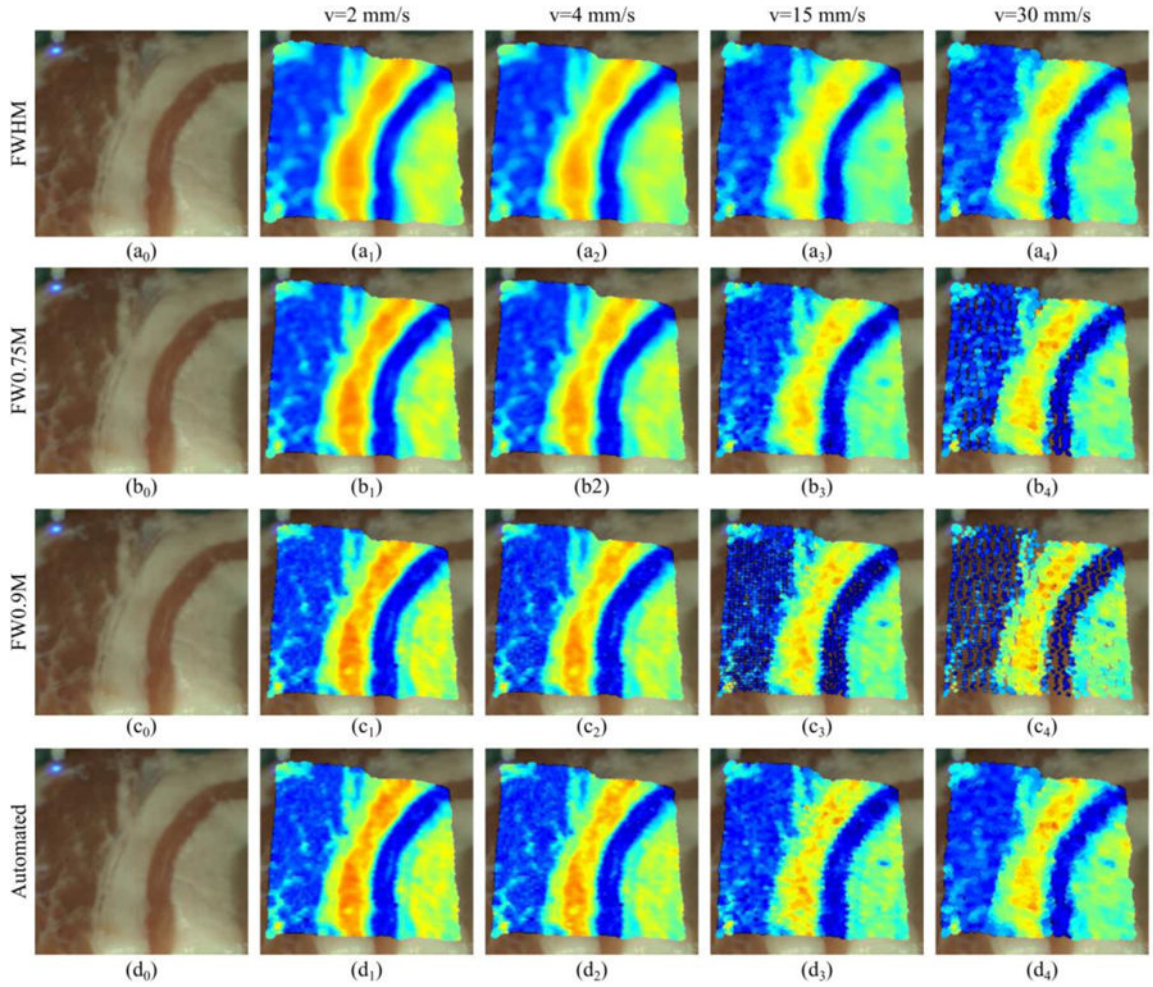

Fig. 8.

Overlay of FLIm maps at 542/50 nm from measurements on fresh porcine tissue sample, index 0, for scanning speeds $v = 2$ mm/s (index 1), $v = 4$ mm/s (index 2) $v = 15$ mm/s (index 3), and $v = 30$ mm/s, (index 4). Overlay was based on FWHM (a), FW0.75M (b), FW0.9M (c), and automated (d) ellipse's scaling. Lifetime values were bounded between 2 ns (blue) and 7 ns (red).

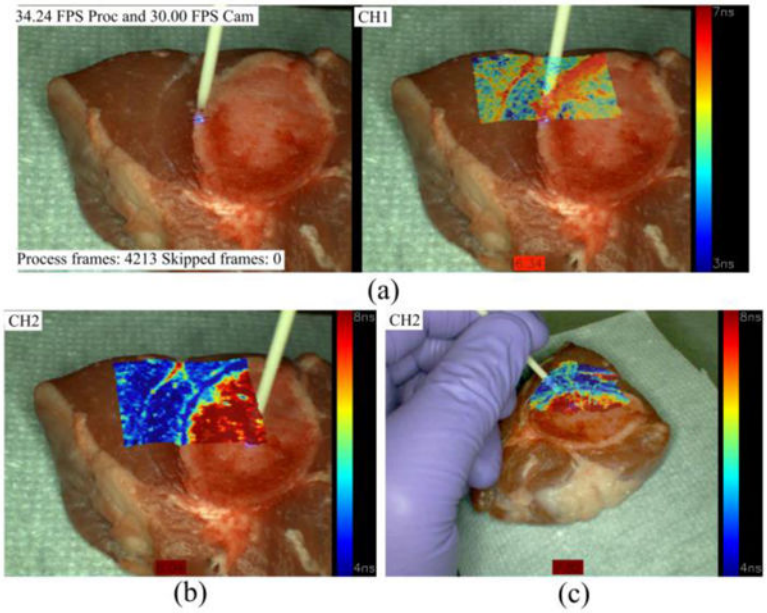

Fig. 9.

Representative GUI screenshots for motorized raster scanning measurements at (a) 390/40 nm and (b) 542/50 nm. The raw video stream is displayed for reference and guidance (a). Information about the scanning parameters is also displayed (a). The scanning process of (a) and (b) can be visualized in the attached video file (clip2). Similarly the overlay at 542/50 nm of handheld scanning at the same tissue is shown in (c). The entire scanning is depicted by the attached video file (clip3).

Table I

Speed Assessment of the Developed Method for Two Frame Resolutions

Algorithmic Block	**Speed (fps)**	
	1280×1024	**640×512**
Image acquisition and resize if needed	77	170
Frame Segmentation	53	70
Formation of all three pseudo-color masks	40	60
Video write to SSD disk	260	370
Acquisition of ms-TRFS signals, preprocessing, TCP/IP transmittance and deconvolution	60	60
Thread group subtotal	33	54
Formation of display image	170	280
Display image	100	120
Total Method	22	34
Camera	17	30
Final Display	17	30